Biomaterials Science

ROYAL SOCIETY OF CHEMISTRY

PAPER

View Article Online
View Journal | View Issue

Cite this: *Biomater. Sci.*, 2025, **13**, 506

A 3D bioprinted adhesive tissue engineering scaffold to repair ischemic heart injury†

Shuai Chen, [a] Lindan Tan,[a] Vahid Serpooshan[b,c,d] and Haifeng Chen*[a]

Received 25th July 2024,
Accepted 21st November 2024

DOI: 10.1039/d4bm00988f

rsc.li/biomaterials-science

Adhesive tissue engineering scaffold (ATES) devices can be secured on tissues by relying on their intrinsic adhesive properties, hence, avoiding the complications such as host tissue/scaffold damage that are associated with conventional scaffold fixation methods like suturing or bioglue. This study introduces a new generation of three-dimensional (3D) bioprinted ATES systems for use as cardiac patches to regenerate the adult human heart. Tyramine-modified methacrylated hyaluronic acid (HAMA-tyr), gelatin methacrylate (GelMA), and gelatin were used to create the hybrid bioink formulation with self-adhesive properties. ATESs were bioprinted and further modified to improve the adhesion properties. In-depth characterization of printing fidelity, pore size, mechanical properties, swelling behavior, as well as biocompatibility was used to create ATESs with optimal biological function. Following *in vitro* testing, the ATESs were tested in a mouse model of myocardial infarction to study the scaffold adhesive strength in biological milieu. The method developed in this study can be used to manufacture off-the-shelf ATESs with complex cellular and extracellular architecture, with robust potential for clinical translation into a variety of personalized tissue engineering and regenerative medicine applications.

Introduction

Tissue engineering scaffolds (TESs) imitate the native tissue extracellular matrix to support cell growth, proliferation, differentiation, and function.[1–3] TESs are applied to injured or diseased tissues as a temporary support to salvage and/or replace the damaged regions and assist in tissue regeneration.[4–6] To fulfill these missions, TES devices must exhibit adequate levels of biocompatibility and bioactivity, pore size distribution (*i.e.*, mass transport properties), mechanical properties, biodegradability, and swelling behavior.[7–9] In conventional clinical applications, TESs are secured into/onto the host tissue through the use of sutures or bioglues, which can introduce multiple issues.[10–14] Suturing might cause secondary damage to the recipient injured tissue, and bioglues could result in adverse structural/functional changes in the scaffolds.[10,15–17] For example, the commonly used cyanoacrylate bioglue has relatively high cytotoxicity and might cause inflammation or exothermic reactions.[18] Fibrin glue, as another example, has insufficient adhesive strength and poses infection risks.[19] In addition to these side effects, bioglues might also block effective interactions between cells from the scaffold, and the native tissues.[15]

To address these issues, adhesive TES (ATES) systems have been developed, offering intrinsic tissue adhesion properties, hence, facilitating the fixation of the scaffold onto the recipient tissue surface without the need of suture or bioglue.[15,20–22] They can circumvent drawbacks of conventional fixation methods and reduce the complexity of application process, particularly for tissues such as cardiovascular system[23] and maxillofacial cartilage,[24] which often introduce deep and constricted geometries and complex structures. In addition, ATESs might be applied through conduits and subsequently adhered to the tissue surface, preventing aggressive operations, such as thoracotomy.[23,25–28]

Current ATES solutions are generally applied to the recipient tissue by casting or injecting pre-gel solutions directly to the target area and *in situ* crosslinking of the solution.[15,22] As a result, these ATESs often lack complex and tailored structural design and geometry. With the advent of additive biomanufacturing technologies, and in particular, 3D bioprinting, TES systems can be fabricated following pre-designed, complex designs.[29–33] 3D bioprinted ATESs could incorporate internal structures, such as vascular network or heterogeneous cell distributions, to enhance the biomimicry, cellular function, and eventually, the engraftment and regenerative efficacy of

[a]*Department of Biomedical Engineering, College of Future Technology, Peking University, Beijing 100871, China. E-mail: haifeng.chen@pku.edu.cn; Fax: +86 10 62754396; Tel: +8610 62754396*
[b]*Department of Biomedical Engineering, Emory University School of Medicine and Georgia Institute of Technology, Atlanta, GA 30322, USA*
[c]*Department of Pediatrics, Emory University School of Medicine, Atlanta, GA 30322, USA*
[d]*Children's Healthcare of Atlanta, Atlanta, GA 30322, USA*
† Electronic supplementary information (ESI) available. See DOI: https://doi.org/10.1039/d4bm00988f

scaffold systems.[20,34,35] Additionally, 3D bioprinting could achieve precise spatiotemporal control on the deposition of cells, small molecules, and biomaterials,[36] and imitation of the distinct tissue geometry (*i.e.*, patient and damage specificity).[37–40]

Among various extrusion-based bioprinting modalities, the embedded or freeform reversible embedding of suspended hydrogels (FRESH) technique allows for bioprinting a wide variety of soft hydrogel-based bioinks *via* the use of a support bath.[41–45] The support medium holds the extruded bioink in place until solidification (curing), hence, offering the opportunity to bioprint highly soft, otherwise non-printable, hydrogel bioinks at adequate fidelity and precision.[41,45] In addition, since bioink formulations at much lower viscosity can be used in the FRESH method, the shear stress imposed on the cells during extrusion can be markedly reduced.[46,47] Among various hydrogel biomaterials used to develop bioink solutions, modified hyaluronic acid (HA) and gelatin are commonly used, as two of the major extracellular matrix (ECM) in the native tissues, hence, offering adequate bioactivity.[48–50]

We recently reported the first generation of ATES devices, created using extrusion-based 3D bioprinting of dopamine-modified methacrylated HA (HAMA-Dopa) and GelMA in both air and Carbopol support bath.[51,52] In this study, a new class of 3D bioprinted ATESs with adequate/optimal manufacturing workflow and adhesive properties was developed for specific use in cardiovascular tissue engineering and regenerative medicine. A novel bioink formulation was developed, containing tyramine-modified HAMA (HAMA-tyr), GelMA, and gelatin. The efficacy of the ATES group with the highest adhesive properties was examined *in vivo* in a mouse model of myocardial infarction (MI) to demonstrate their potential for clinical applications.

Experimental procedures

Materials

HA, methacrylic anhydride (MA), 1-ethyl-3-(3-dimethylaminopropyl) carbodiimide (EDC), *N*-hydroxy succinimide (NHS), sodium hydroxide (NaOH), hydrochloric acid (HCl), ethanol, deuterium oxide, gelatin, and phosphate buffer solution (PBS) were all purchased from Sigma (USA). Tyramine hydrochloride, H_2O_2 solution, horseradish peroxidase, dimethylbenzene, and paraffin were purchased from Aladdin (China). Carbopol was purchased from Lubrizol (USA). Genipin was purchased from Energy Chemical (China). Lithium phenyl-2,4,6-trimethylbenzoylphosphinate (LAP) was purchased from Engineering for Life (China). Formaldehyde solution was purchased from Solarbio (China). Masson staining kit, neutral balsam, and the cell counting kit (CCK-8) were purchased from Yeasen (China). Complete medium for L929 cells was purchased from Procell (China). Cell freezing medium was purchased from NCM Biotech (China). Live/Dead assay kit was purchased from Abbkine (USA).

Animals

8- to 10-week-old male C57/6J mice were purchased from the laboratory animal center of Peking University (China) and utilized following the rules and regulations of Animal Care and Use Committee at Peking University, as described previously.[53]

Synthesis of functional hydrogel-based bioink

Synthesis of HAMA

Following a published protocol,[54] 1 g of HA was dissolved in PBS solution at 1 wt% concentration. Next, 19 mg ml^{-1} of MA was added to the solution in a drop-by-drop manner under vigorous stirring. The pH of the mixture was set to be 8–11 with the help of a 5 M NaOH solution. The stirring continued until the MA drops were dispersed uniformly in the HA solution. Then, the system was maintained at 4 °C for 24 hours. Following the reaction, the solution was added to cold ethanol. The white precipitate was obtained by centrifuge under 9500 RPM for 10 min to remove the supernatant. The precipitate was re-added to cold ethanol and centrifuged again. The process was repeated three times, and the final product was dialyzed for three days against distilled water. The product was then freeze-dried for three days and stored at −20 °C until use.

Synthesis of HAMA-tyr

Following a published protocol,[55] 1 g of HAMA was dissolved in PBS solution at 1 wt% concentration. Next, 7.2 mg ml^{-1} of EDC, 4.3 mg ml^{-1} of NHS, and 5.2 mg ml^{-1} of tyramine hydrochloride were added to the system, and the reaction was allowed to continue for 10 hours under the pH of 7 at room temperature while being stirred. After three days of dialysis against distilled water, the solution was freeze-dried and stored at −20 °C until use.

Synthesis of GelMA

20 g of gelatin was dissolved in 200 mL PBS solution and the system was heated to 50 °C. Next, 0.2 g of MA was added to the system 10 times, with the total amount of 2 g MA added to the solution. After each MA addition, the pH of the solution was adjusted to 8–11. After 2.5 hours, the reaction was stopped by lowering the pH of the solution down to 7 using 5M HCl solution. The system was diluted with 400 mL PBS solution preheated to 50 °C and was filtered using a 0.2 μm syringe filter to remove precipitates. The solution was then dialyzed for three days against distilled water and freeze-dried for another 3 days to obtain the final GelMA product.[56]

^{1}H NMR spectroscopy

The hydrogel components (HA, HAMA, HAMA-tyr, gelatin, and GelMA) were dissolved in deuterium oxide at the concentration of 5 mg ml^{-1} and the solution was freeze-dried. The dried components were re-dissolved in deuterium oxide and freeze-

dried again. The process was repeated three times in total to reduce the peak height from hydrogen oxide. The obtained products were dissolved in deuterium oxide at the concentration of 5 mg ml^{-1} and the solutions were transferred to NMR tubes to perform ^1H NMR spectroscopy using a 500 MHz spectrometer (Bruker, US).

In the NMR spectrum acquired for HA, HAMA and HAMA-tyr, the peaks at 5.6 and 6.1 ppm represented the methacrylate protons ($Area_1$), the peak at 6.8–7.2 ppm was from the 4 phenyl protons of tyramine groups ($Area_2$), and the peak at 1.9 ppm represented *N*-acetyl glucosamine of HA ($Area_3$ in the spectrum of HAMA and $Area_4$ in the spectrum of HAMA-tyr). The degree of substitution of MA group to the backbone of HA ($D_{MA\text{-}HA}$) was calculated by the following equation:

$$D_{MA\text{-}HA} = \frac{3 \times Area_1}{2 \times Area_3} \quad (1)$$

The degree of substitution of dopamine group to the backbone of HAMA (D_{tyr}) was calculated by the eqn (2):

$$D_{tyr} = \frac{3 \times Area_2}{4 \times Area_4} \quad (2)$$

In the NME spectrum for gelatin and GelMA, the peaks at 2.8–2.95 ppm ($Area_5$) represented lysine methylene protons from the unreacted lysine groups of the gelatin and peaks at 5.2–5.7 ppm ($Area_6$) represented acrylic protons of methacrylate groups. The degree of substitution of MA group to the backbone of gelatin ($D_{MA\text{-}gelatin}$) was calculated using the eqn (3):

$$D_{MA\text{-}gelatin} = \frac{Area_6}{Area_5 + Area_6} \quad (3)$$

Embedded (FRESH) 3D bioprinting process to create ATES systems

Carbopol support bath preparation

To prepare the support bath, 0.8% Carbopol was added to distilled water and stirred for 24 hours. Then 0.75% genipin and 2 mM H_2O_2 were added to the system, which was stirred for another 1 hour. The pH of the system was adjusted to 7 and the mixture became viscous. The Carbopol support bath was stored at 4 °C until use.

Bioink preparation

0.25% HAMA-tyr, 5% GelMA, and 5% gelatin were dissolved in distilled water, and then 10 U ml^{-1} horseradish peroxidase and 0.25% LAP were added to the solution. The bioink was kept at 4 °C until use.

ATES biofabrication workflow

CAD software was used to create the 3D digital models. The bioink was extruded and printed layer by layer into the support bath based on the 3D model, and then solidified overnight in the Carbopol support. ATESs were extracted from the support bath with the help of PBS solution. Subsequently, the scaffolds were coated with dopamine by immersing the constructs in 0.01 g mL^{-1} dopamine solution for 10 minutes. The surface of the ATESs were next dehydrated (to remove excess water) at 37 °C for 10 minutes. For the *in vitro* adhesion testing, a dried collagen sheet (The Sausage Maker, USA) was used as the adhesion substrate, imitating the recipient tissue. The modified ATESs were applied and adhered to the substrate surface. The vinyl groups were initiated by blue light for 30 seconds to enhance the interaction with moieties on tissue surface, resulting in an increase in the adhesion properties. Experimental conditions for different groups are listed in Table 1.

Bioprinting fidelity analysis. The fidelity of embedded bioprinting was examined in both micro- and macro- (bulk) scales based on previously published protocols.[37,52,57,58] For the measurement of micro fidelity, the bioink was extruded on a glass slide based on a lattice pattern and ImageJ software was used to measure the diameter of the lines, the angle between two crossed lines, and the area entrapped within the printed lines. The percentage ratios between the print *versus* CAD model were calculated for the line diameter ($r_{diameter}$), angle (r_{angle}), and area (r_{area}) using the following equations to represent the micro-fidelity of embedded printing:

$$r_{diameter} = \frac{d_{print,micro}}{d_{model,micro}} \times 100 \quad (4)$$

where $d_{print,micro}$ is the diameter of the printed lines and $d_{model,micro}$ is the diameter of lines in the original CAD model.

$$r_{angle} = \frac{\alpha_{print,micro}}{\alpha_{model,micro}} \times 100 \quad (5)$$

where $\alpha_{print,micro}$ is the angle between the printed lines and $\alpha_{model,micro}$ is the angle between lattice lines in the original CAD model.

$$r_{area} = \frac{A_{print,micro}}{A_{model,micro}} \times 100 \quad (6)$$

where $A_{print,micro}$ is the surface area between the printed lines and $A_{model,micro}$ is the surface area between lattice lines in the original CAD model.

For the measurement of macro (bulk) fidelity of embedded printing, a 3D model of letter "P" was created using CAD software and used to bioprint the ATES constructs. Using ImageJ, the surface area, length, width, and perimeter of the bioprinted ATESs were measured, and their ratios were calculated based on those of the CAD model using the following equations:

$$R_{length} = \frac{L_{print,macro}}{L_{model,macro}} \times 100 \quad (7)$$

where R_{length} is the ratio (percentage) of the length of the printed scaffold ($L_{print,macro}$) to that of the original CAD model ($L_{model,macro}$).

$$R_{width} = \frac{W_{print,macro}}{W_{model,macro}} \times 100 \quad (8)$$

Table 1 Experimental conditions used for biofabrication of ATES constructs in this study

Groups	Ingredients	Concentration	Printing and crosslinking condition	Post-printing modifications
Unmodified	HAMA-tyr/gelatin/GelMA	0.25%/5%/5%	Embedded printing – overnight in support bath	None
Dehydrated	HAMA-tyr/gelatin/GelMA	0.25%/5%/5%	Embedded printing – overnight in support bath	10 min dehydration under 37 °C
Dehydrated/DOPA-coated	HAMA-tyr/gelatin/GelMA	0.25%/5%/5%	Embedded printing – overnight in support bath	10 min immersion in 0.01 g ml^{-1} dopamine hydrochloride solution and 10 min dehydration under 37 °C
Dehydrated/DOPA-coated/light exposure	HAMA-tyr/gelatin/GelMA	0.25%/5%/5%	Embedded printing – overnight in support bath	10 min in 0.01 g ml^{-1} dopamine hydrochloride solution, 10min dehydration at 37 °C, and blue light exposure after adhesion

where R_{width} is the ratio (percentage) of the width of the printed scaffold ($W_{print,macro}$) to that of the original CAD model ($W_{model,macro}$).

$$R_{perimeter} = \frac{P_{print,macro}}{P_{model,macro}} \times 100 \quad (9)$$

where $R_{perimeter}$ is the ratio (percentage) of the perimeter of the printed scaffold ($P_{print,macro}$) to that of the original CAD model ($P_{model,macro}$).

$$R_{Area} = \frac{A_{print,macro}}{A_{model,macro}} \times 100 \quad (10)$$

where R_{Area} is the ratio (percentage) of the surface area of the printed scaffold ($A_{print,macro}$) to that of the original CAD model ($A_{model,macro}$).

Evaluation of mechanical properties of 3D bioprinted ATES constructs. A mechanical tester (AGS-X, Shimadzu, Japan) equipped with a cylindrical probe, was used for mechanical analysis of ATES constructs. The height of the scaffolds was measured by lowering the upper probe until the upper surface of the ATES got in touch with the probe. The height was determined as the distance between the lower surface of the probe and the upper surface of the platform. The probe pressed the scaffolds at a steady speed of 1 mm s^{-1} under the control of the mechanical tester until the loading force of the probe reached 5 N. The load-displacement data was recorded by the mechanical tester and the stain-stress relationship was calculated using the following equations:

$$\text{Stress} = \frac{\text{load}}{\text{initial scaffold cross sectional area}} \quad (11)$$

$$\text{Strain} = \frac{\text{displacement}}{\text{initial scaffold height}} \quad (12)$$

The Young's modulus was calculated from the slope of the strain-stress curve for each study group at the 9–11% of displacement interval.

Measurement of swelling behavior of 3D bioprinted ATES constructs. The weight of ATES samples from each group was measured and recorded right after printing ($W_{t=0}$). Scaffolds were then transferred to a cell culture dish and submerged in PBS solution. At certain intervals, the scaffold weight was measured and recorded (W_t). Every other day, the liquid in the cell culture dish was discarded and replaced with fresh PBS solution. The swelling behavior of ATESs was represented by the weight ratio of the scaffold after and before immersing in PBS solution and was determined as a percentage (WR) using the following equation:

$$WR = \frac{W_t}{W_{t=0}} \times 100 \quad (13)$$

Pore size analysis of embedded bioprinted ATES constructs. ATESs (sliced in half and full construct) were rapidly frozen in liquid nitrogen for 45 seconds and then freeze-dried. The scaffolds were next adhered to a copper tape fixed on a plate and the surface or the cross section of the ATESs were sput-

tered for 90 seconds with gold particles under 120 mA. The scaffolds were examined by SEM (Quanta FEG 45, FEI, USA) to analyze the pore size distribution on the surface as well as at the cross section of the constructs. ImageJ was used to measure the pore size. The data was then analyzed using Origin software to create a histogram illustrating the pore size distribution. The distributions were fitted into a nonlinear curve based on Lognormal function. In addition, a nonlinear curve based on the Boltzmann function was used to match the cumulative pore size frequencies. Based on the cumulative frequency curve, the pore sizes corresponding to d_{10}, d_{50}, and d_{90} (where d_n denotes the diameter of pores larger than n% of all pores) were measured.

Evaluation of *in vitro* adhesion properties of bioprinted ATESs. The *in vitro* adhesive properties were determined with the help of a mechanical tester (AGS-X, Shimadzu, Japan), which was equipped with two symmetrical clamps. Two T-shaped aluminum alloys were clamped onto the machine symmetrically. A piece of collagen sheet was glued to one of the aluminum alloys, and the ATES was then adhered to the collagen sheet. The opposite side of the ATES was glued to the other aluminum alloy. During the adhesion test, the mechanical tester gradually drew the aluminum parts apart at the speed of 3 mm s^{-1} until the bonding between the ATES and the collagen sheet broke. The maximum stress that the bonding could withstand under tensile stress ($AS_{tensile}$) was recorded as adhesive strength for each study group, using the following equation:

$$AS_{tensile} = \frac{load_{max}}{area} \quad (14)$$

where $load_{max}$ is the maximum load that the bonding could tolerate and *area* is the adhesion surface area between the ATES and the collagen sheet.

Measurement of cytotoxicity of the bioprinted ATESs (CCK-8 test). Mouse fibroblast (L929) cells were cultured in tissue culture plates for three days in complete cell culture medium (MEM + NEAA + 10% FBS + 1% P/S) at 37 °C and 5% CO_2. The media was changed every other day. ATESs were exposed to UV light for 1 h for sterilization and then incubated in cell culture media at the concentration of 10% (0.1 g ATES in 1 mL culture medium) for 24 h at 37 °C. The extractions (collected from supernatant media) were sterilized by passing through a syringe filter with 0.2 μm pore size. L929 cells were seeded at a density of 3×10^5 cells per well in 96-well plates and incubated overnight in 100 μL per well of cell culture medium. After discarding the cell culture medium, 100 μL of extraction was added to each well. For the control group, complete cell culture media was added. The extraction and cell culture media were replaced every other day. At certain time intervals, the media in each well was removed and 100 μL of fresh cell culture medium with 10% CCK8 kit reagent was added. The whole plate was incubated at 37 °C for 1 h before being analyzed using a microplate reader. The optical density (OD) under 450 nm was measured.[59,60] The OD ratio (OD_{ratio}) of experimental groups (cultured with extraction media) to the control group (cultured with fresh and complete media) was calculated using the following equation as a measure of ATES cytotoxicity:

$$OD_{ratio} = \frac{OD_0}{OD_1} \quad (15)$$

where OD_0 is the optical density of the experimental group (cultured with the extraction media) and OD_1 is the optical density of the control group.

Live/Dead assay. ATESs were UV-sterilized for one hour and then put in 24-well culture plates. Next, 5×10^5 cells per mL of L929 cells were seeded onto the ATES samples and cultured at 37 °C with 5% CO_2 for 6 h to ensure cell attachment. Following this period, the media was discarded, and 1 mL of fresh complete cell culture medium (MEM + NEAA + 10% FBS + 1% P/S) was added to each well. The culture media was changed every other day. ATESs were collected for examination at selected time points.

The Live/Dead assay reagents were diluted with 1× PBS to the concentration of 1 μL ml^{-1}. Each ATES was cultured in 1 mL of the solution for 30 minutes in an incubator covered with aluminum foil before being examined with a fluorescence microscope for imaging and quantification.[61,62]

Evaluation of *in vivo* adhesive properties of bioprinted ATES constructs

The creation of the myocardial infarction (MI) model

Animal studies were conducted following the regulations approved by the Institutional Animal Care and Use Committee (IACUC) of Peking University. Our team had received the approval from the IACUC to conduct the animal experiments. The mouse model of sham and MI was created following the protocol of our lab which was published in an article.[63] Briefly, mice were placed in the chamber of anesthesia machine, and 3% anesthetic (isoflurane) was applied for one minute. After being rendered unconscious, the mice were placed on the operating table. Depilatory cream was rubbed over the mouse chest, and the chest hair was shaved to expose the surgical region. The ventilator was activated, and the glottis of the mouse was cut open. An endotracheal tube was inserted along the trachea to link the mouse to the ventilator. The chest cavity of the mouse was opened by cutting the tissues between the third and fourth costa, and the heart was exposed to its entirety. Experimental groups included: the sham operated mice (no MI, no patch), the MI mice without ATES treatment (control), and MI mice treated with ATES patch (main study group). To induce the MI, the position of the left coronary artery (LAD) was identified; an Surgical needle was penetrated in the tissue at the lower edge of the left atrial appendage. The LAD artery was blocked by a suture to totally obstruct its blood supply. For the sham group, the chest cavity of the mouse was closed without ligating the LAD artery. For the sham, MI-only,

and MI treated with ATES patch group, one mouse was used for each group.

Applying the ATESs onto the MI tissue

For the experimental group treated with patch, the ATESs were adhered to the epicardial surface of the heart to fully cover the infarct and *peri*-infarct regions. Subsequently, the ATES patch was exposed to the blue light for 10 seconds to initiate the MA groups and effective adherence. The thoracic aperture was then thoroughly closed. For the control group (MI without patch), after ligating the LAD artery, the thoracic aperture was closed immediately with sutures. After surgery, the endotracheal tube was withdrawn from the trachea, and the mice were carefully monitored for respiratory problems. Animal studies continued for 4 weeks.

Termination of *in vivo* experiments – analysis of adhesive conditions of the implanted ATESs

At week 4 post grafting, the mice were euthanized through spinal dislocation. The rear of the mouse was pushed by the right hand, while the head was depressed by the thumb and index finger of the left hand. Subsequently, the thoracic cavity was reopened, and the mouse heart was revealed. In the patch-treated group, the surgical location, geometry and structure, and bonding condition of the ATES onto the myocardial tissue were carefully examined and photographed. The heart was then harvested, washed with cold saline solution, and then underwent slicing and histological analyses.

Heart tissue processing and Masson's trichrome staining

Extracted heart tissues were fixed by immersing in 4% formaldehyde solution for 48 hours. The tissue was then dehydrated in 70% ethanol for 6 hours, 80% ethanol for 20 minutes, 90% ethanol for 20 minutes, and anhydrous ethanol for 15 minutes (2X). The dried sample was then immersed in dimethylbenzene and placed in molten paraffin at 55–62 °C for 1 hour. The sample was then thoroughly cooled and mounted on the rotary microtome for slicing into thin films at 3–4 μm thickness. Tissue slices were placed in 37 °C water bath to be flattened, then loaded onto glass slides and heated overnight at 37 °C to permanently adhere onto the slides. After dewaxing, the slides were stained with Masson's trichrome staining kit. The slides were naturally dried and examined with an optical microscope (CKX41, Olympus, Japan). After staining, connective tissue appeared in red and collagen fibers appeared in blue.

Statistical analysis. All measured data were reported as mean values ± standard deviation (SD). The statistical significance was examined by *T*-test, one-way or two-way analysis of variance. Multiple comparisons were performed using Tukey test by GraphPad Prism with an acceptable significance level of $p < 0.05$. In this study, $^{*}p < 0.05$, $^{**}p < 0.01$, and $^{***}p < 0.001$ in comparison to the groups of control or reference.

Results and discussion

Traditionally, TES devices are applied to the recipient tissues and organs *via* the use of bioglues and/or sutures.[15,64] However, these methods often cause side effects, such as secondary damage or possible toxicity and/or infection.[18,19,65] ATESs offer an alternative route for securing biomaterials onto the tissues without the need for such aggressive operations.[15,20] Previously reported ATES designs are based on amorphous hydrogel systems,[26,56,66,67] electrospun constructs,[68] or non-hydrogel foams,[69] which all lack the capability of creating complex structures and heterogenous cellular/biomaterial architectures. 3D bioprinting methods could help to incorporate sophisticated designs, such as vascular network or hollow structures,[70] cell/cell factor patterning,[71] imitating the native tissue structure,[72] or patient-specific geometries.[40]

The adhesion strength of ATES systems onto tissue surfaces is based on molecular interactions, including covalent, ionic, hydrogen, van der Waals, and hydrophobic bonding, as well as polymeric interactions, including chain interpenetration and entanglement.[73] In this study, the adhesive properties of ATESs were further enhanced by post-printing modifications including dopamine coating and surface dehydration. Dopamine groups could form chelation with the recipient tissue surface through interaction between phenols of dopamine groups and hydroxyl, thiol, or amine groups from the host tissue.[66,74] Surface dehydration could remove water molecules from the surface of ATES, hence reducing the water boundary, which forms a barrier between the scaffold surface and the recipient tissue and therefore impedes molecular interactions.[75,76] After grafting onto the tissue surface, the ATESs were exposed to blue light to trigger the MA groups on the backbone of GelMA and HAMA-tyr, to react with amine or hydroxyl groups on the tissue surface, hence, increasing the adhesion strength.[56]

ATESs were fabricated using an embedded (FRESH) 3D bioprinting method (Fig. 1). Bioink was printed and solidified within the support bath (Fig. 1B). Bioprinted ATES was harvested from the Carbopol bath after crosslinking and was modified by dopamine coating and surface dehydration to increase the adhesion property (Fig. 1C). After applying the scaffold onto the substrate, the ATESs were exposed to light for MA group initiation (Fig. 1D). The adhesion of ATESs to substrates was the result of the reaction of initiated MA groups with the moieties on the substrate surface, as well as the chelation and electric interactions formed between the dopamine groups and functional groups on the substrate (Fig. 1E).

Among various hydrogel components to create bioinks, we chose modified HA and gelatin considering their well-established characterization and use in tissue bioprinting as common native ECM components with adequate biocompatibility and bioactivity.[45,49,77] Successful modification of HA with MA groups was confirmed by the NMR spectra of HA and HAMA (Fig. 2A). The peak at 1.9 ppm corresponds to the proton of *N*-acetyl glucosamine of HA, whereas the peaks at 5.6

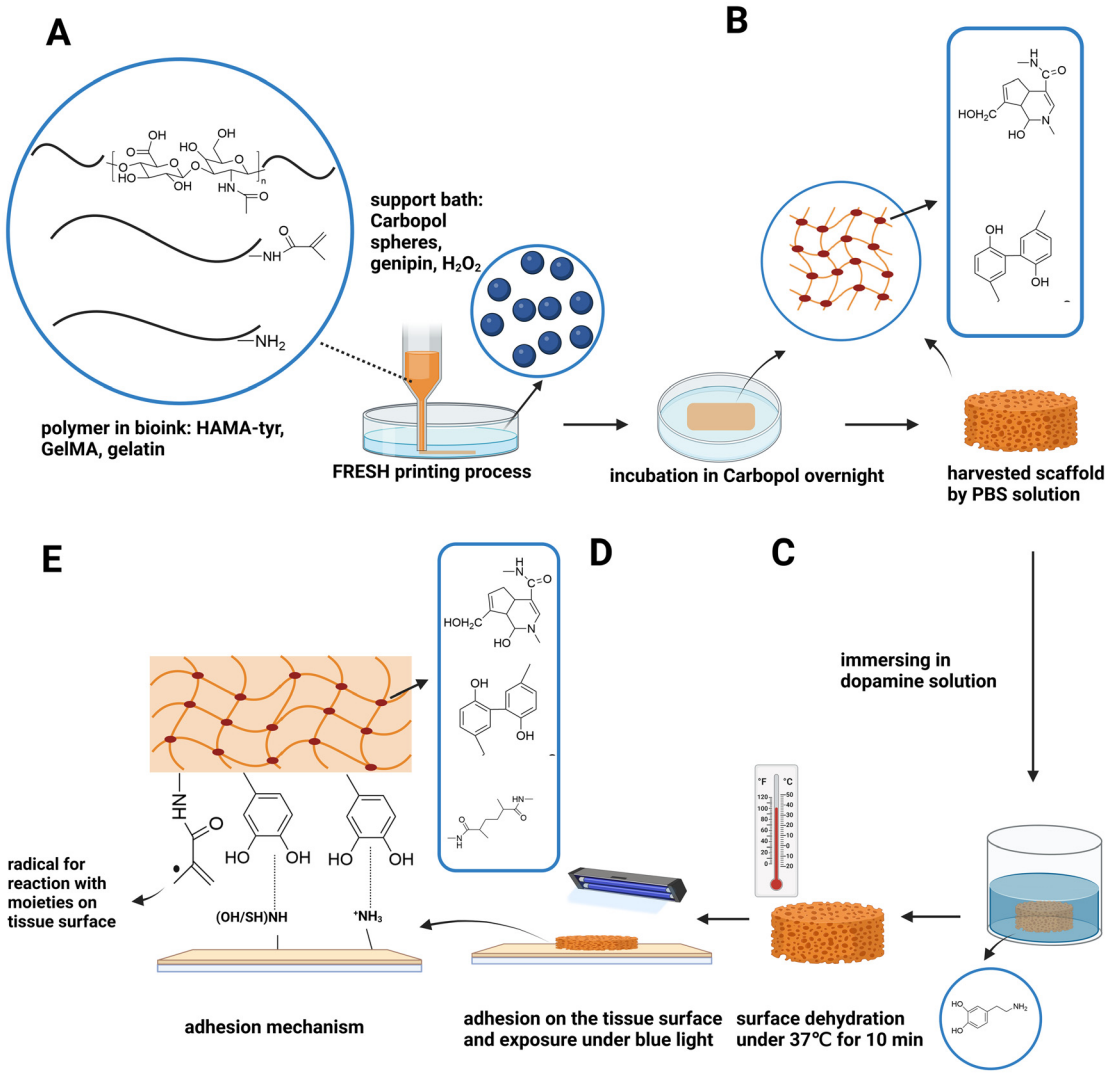

Fig. 1 The workflow used for fabricating adhesive tissue engineered scaffolds (ATESs) through embedded 3D bioprinting. (A) Bioinks comprised of Tyramine-modified methacrylated hyaluronic acid (HAMA-tyr), gelatin, and gelatin methacrylate (GelMA) were prepared and used to bioprint the scaffold within a Carbopol support bath. Printed ATES was then solidified within the bath, harvested using PBS solution (B), and modified by dopamine coating, surface dehydration (C), and light exposure while applied to the substrate to improve the adhesion properties (D). (E) Schematic illustration of various mechanisms involved in the adhesion of ATES to the substrate.

and 6.1 ppm represent protons from MA groups. The degree of modification was measured at 49.34%. Tyramine groups were modified to the HAMA backbone, resulting in the peak at 6.8–7.2 ppm in the HAMA-tyr spectrum, corresponding to the 4 phenyl protons from tyramine groups (Fig. 2A).[54,55] The degree of modification of tyramine groups was calculated at 18.98%.

The modification of gelatin with MA groups was also confirmed with the NMR spectra of gelatin and GelMA (Fig. 2C). The peak at 2.8–2.95 ppm reflects protons of lysine methylene from unreacted lysine groups on the gelatin backbone, whereas the peak at 5.2–5.7 ppm represents acrylic protons from MA groups modified to gelatin chains.[78,79] The degree of modification was measured at 84.75%. Modified hydrogels were dissolved in aqueous solution for the preparation of bioink, and were crosslinked using multiple mechanisms (Fig. 2B and D).

Micro- and macro- (bulk) scale fidelity of the 3D bioprinted ATES constructs examined the accuracy of scaffold fabrication processes. For the measurement of micro fidelity, a square lattice geometry was printed on glass slides (Fig. 3A–D). The fidelity ratios for the diameter, angle, and area of bioprinted strands were measured at 108.5 ± 5.8%, 100.8 ± 2.2%, and 93.4 ± 4.2%, respectively (Fig. 3D). The printed strand diameters were larger than those of the model, likely due to the swelling behavior, surface tension of the bioink, and gravity force causing deformation/collapse of the deposited hydrogel.[80–82] The strand angles were close to 90°, representing adequate angle accuracy. The areas between two sets of parallel strands were slightly smaller than that of the model. This could be

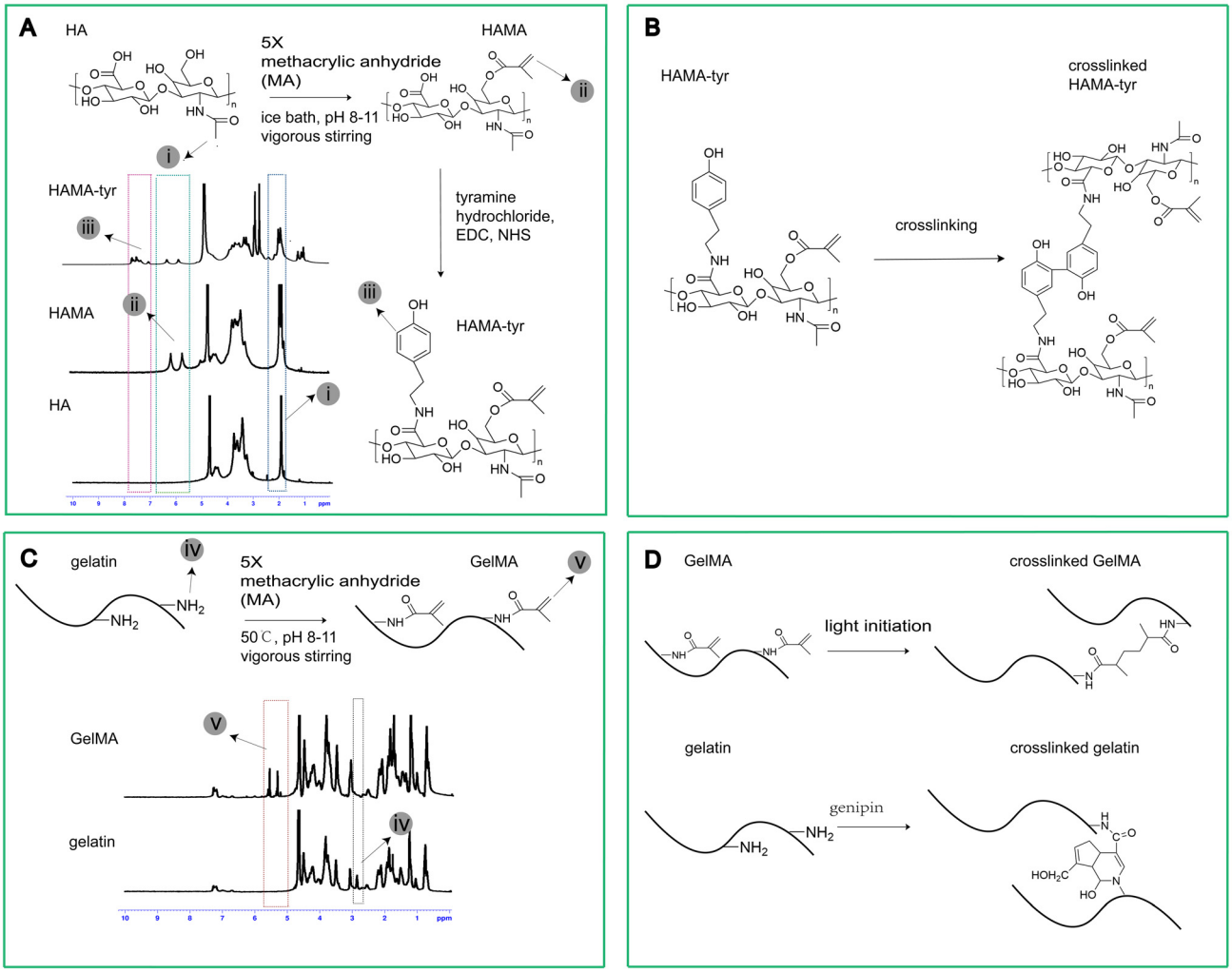

Fig. 2 Preparation of various bioink components and their nuclear magnetic resonance (NMR) spectroscopy analysis. (A) The preparation and NMR spectra of HA, HAMA, and HAMA-tyr. Protons from the *N*-acetyl glucosamine of HA (i), methacrylate of MA groups (ii), and benzene ring of the tyramine group (iii) are demonstrated. (B) Crosslinking of HAMA-tyr in the support bath post bioprinting. (C) The preparation and NMR spectra of gelatin and GelMA. Protons from the remaining lysine methylene of the unreacted lysine group (iv) and acrylic from the methacrylate groups (v) are shown. (D): The crosslinking of GelMA by the reaction between the MA groups under blue light and the crosslinking of gelatin by the reaction between amine groups initiated by genipin.

attributed to the increased diameters of the printed strands and a degree of extruded ink fusion/melting particularly at the corners the printed pattern.[45]

The bulk (macro-scale) fidelity of bioprinting was examined by printing a 3D construct based on the digital model (Fig. 3E and H). The fidelity ratios for the 3D construct's length, width, perimeter, and area were measured at 97.4 ± 1.3%, 98.3 ± 5.6%, 107.3 ± 1.6%, and 105.0 ± 1.4%, respectively (Fig. 3H), indicating relatively high printing accuracy. Infiltration of extruded bioink into the void spaces within the surrounding Carbopol particles is likely a major contributing factor to the uneven outline and divergence from the CAD design.[43] The length and width of the bioprinted scaffold were slightly smaller than those of the CAD model, likely because of the resistance of the Carbopol bath that reduced the flow rate of the bioink. The perimeter of the printed scaffolds was larger than that of the model, which might be the consequence of non-ideal micro-fidelity in printing strands. Together, these results demonstrated relatively high levels of bioprinting fidelity for the soft, adhesive, hydrogel-based bioink, both at the micro- and macro-scales.

The adhesive strength of bioprinted ATES constructs was first measured in dry conditions (in air) at 1.1 ± 0.1 kPa, 2.2 ± 0.1 kPa, 4.4 ± 1.5 kPa, and 5.5 ± 2.2 kPa, for the unmodified, dehydrated, dehydrated/DOPA-coated, and dehydration/DOPA-coated/photo-activated groups, respectively (Fig. 3I–K). The ATES surface was dehydrated to remove superficial water molecules which could form a barrier between the functional groups on the surface of the tissues and the ATES, interfering with their interactions.[75,76] Hence, reducing the water barrier could enhance the adhesive properties of ATES. In the dehydrated/DOPA-coated group, in addition to dehydration,

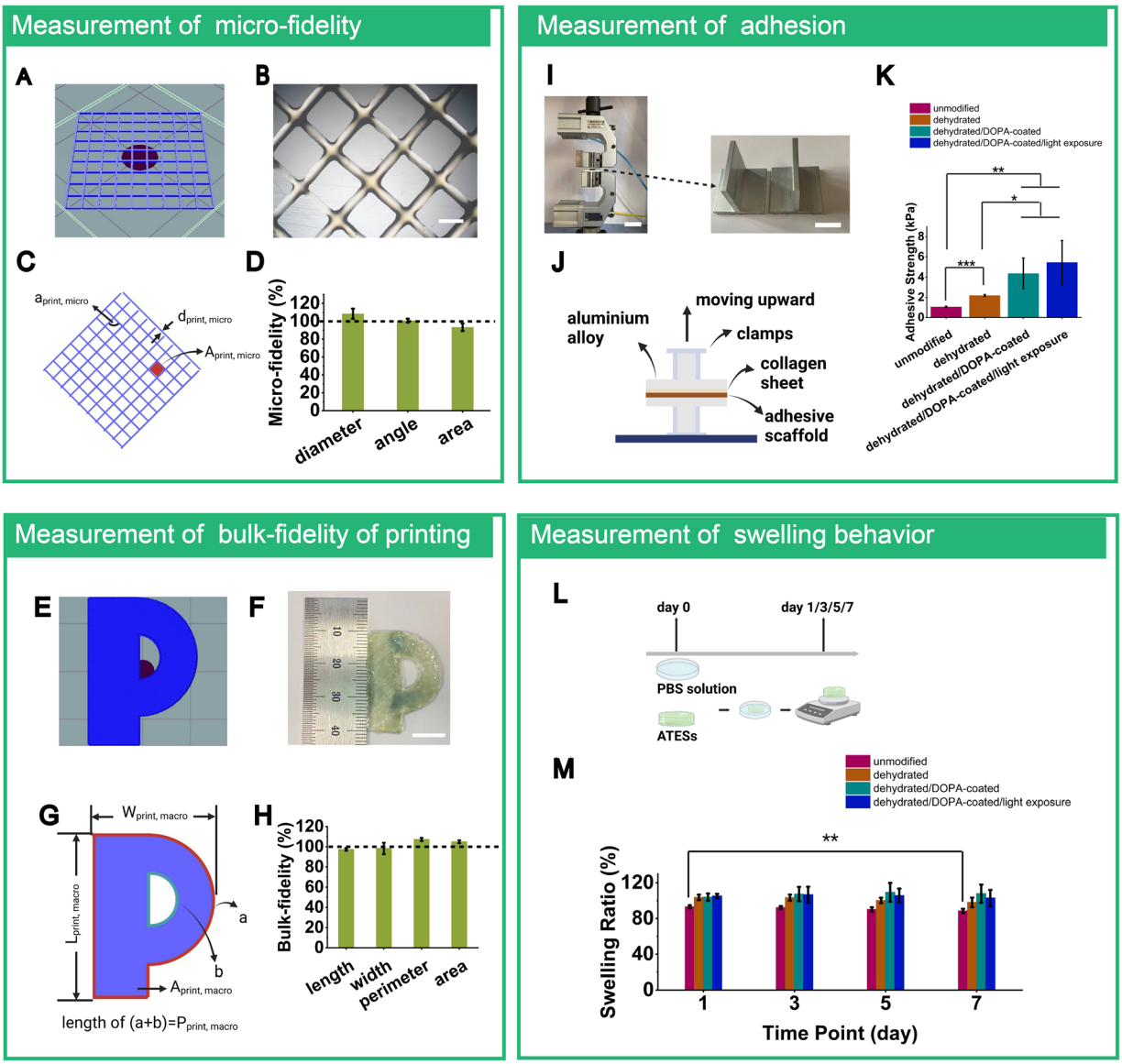

Fig. 3 The fidelity analysis for the hybrid bioink and 3D embedded bioprinting method utilized in this study to fabricate adhesive tissue engineered scaffolds (ATESs). (A)–(C) The computer aided design (CAD) model and the photograph of 2D lattice pattern used for micro-scale fidelity measurement of embedded bioprinted bioink. The scale bar represents 1 mm. The parameters measured for fidelity are shown in (C), with $d_{print,micro}$ as the diameter of the printed strands, $\alpha_{print,micro}$ as the angle between the lines, and $A_{print,micro}$ as the areas between the two sets of parallel strands. (D) The fidelity ratios calculated for various parameters of the printed pattern, normalized by those of the CAD model (n = 12). (E–G) The CAD model and photograph of the letter "P" used for the measurement of macro-scale (bulk) fidelity of embedded bioprinting. The scale bar represents 10 mm. The structural parameters (width, length, and perimeter) used to assess bulk fidelity are shown in (G). (H) The fidelity ratios were calculated by dividing the bulk parameters of bioprints to those of the CAD model (n = 3). (I) The mechanical testing stress. Scale bars represent 30 mm and 15 mm in the left and right panels. (J) The schematic illustration of the experimental set-up used to assess the adhesive properties. (K) The adhesion strength of various study groups under tensile stress (n = 4). *p < 0.05, **p < 0.01, and ***p < 0.001. (L) The timeline used for measuring swelling behavior of ATESs. (M) Measured weight ratios of ATESs for different study (n = 4). *p < 0.05, **p < 0.01, and ***p < 0.001.

scaffolds were coated with dopamine groups, which could form chelation with functional groups such as hydroxyl, amine, or thiol groups on tissue surfaces to further improve the adhesion strength.[66,83] In the final study group, the ATESs were exposed to blue light after surface modifications and application to the substrate, which initiated MA groups to generate radicals and react with moieties on the substrate surface, resulting in increased adhesive strength.[56] These *in vitro* results suggested that the ATES group that underwent a combination of dehydration, dopamine coating, and photoactivation of MA groups, exhibited the highest levels of adhesive strength (Fig. 3K).

The swelling behavior of ATES in aqueous milieu was also examined to further determine the functionality of such

scaffolds in the *in vivo* applications (Fig. 3L and M). The weight ratios of unmodified ATES group were 93.2 ± 1.8%, 92.3 ± 1.6%, 90.2 ± 2.4%, and 88.5 ± 2.3% on days 1, 3, 5, and 7, respectively (Fig. 3M). The scaffold weight slightly reduced over time, likely as the result of the released Carbopol particles from the constructs. During the embedded bioprinting process, Carbopol particles may penetrate the scaffold and partially remain in the 3D structure after harvesting. In addition, uncrosslinked polymers might also be released from the ATESs, contributing to the weight reduction.[45,84] The weight ratios of dehydrated scaffolds were measured at 103.7 ± 3.1%, 103.5 ± 3.4%, 100.3 ± 3.0%, and 98.0 ± 5.3% on days 1, 3, 5, and 7, respectively (Fig. 3M). The weight of ATESs rose marginally before decreasing, which is likely due to the re-absorption of water after surface dehydration. The weight ratios for the dehydrated/DOPA-coated group were at 104.0 ± 4.0%, 107.4 ± 8.0%, 109.4 ± 10.5%, and 107.9 ± 10.2% on days 1, 3, 5, and 7, respectively (Fig. 3M). The coating of dopamine improved the hydrophilicity of ATES, which likely caused a higher weight gain.[85,86] Finally, the weight ratios for the scaffold group treated with dehydration/DOPA-coating/photo-activation were measured at 105.2 ± 2.3%, 106.7 ± 8.9%, 105.7 ± 7.8%, and 103.0 ± 9.0% on days 1, 3, 5, and 7, respectively (Fig. 3M). The enhanced crosslinking density from vinyl group reaction was likely the reason for the reduced weight gain in this group, compared with the previous group.[87] Overall, relatively small-scale swelling was observed in all ATES groups, highlighting the ability of these bioprinted scaffolds for maintaining their shape/structural integrity in the *in vivo* (wet) applications.

The mechanical properties of ATESs should be comparable to those of the native tissues that will receive the scaffold. Cell attachment, differentiation, and function would also be significantly influenced by the mechanical properties of these scaffolds. The tissue stiffness in human body typically ranges from <0.1 kPa, in the brain, to 20 GPa in the bone tissue.[88] To assess the mechanical characteristics of bioprinted ATES systems, stress–strain data representing the mechanical strength of scaffolds were obtained (Fig. 4A). Young's modulus which was calculated at 18.3 ± 2.0 kPa, 18.5 ± 2.4 kPa, 18.4 ± 0.8 kPa, and 20.6 ± 1.1 kPa, for the unmodified, dehydrated, dehydrated/DOPA-coated, and dehydration/DOPA-coated/photo-activated groups, respectively, without significant differences across groups (Fig. 4B). The slight increase in Young's modulus (stiffness) of the final group is likely due to higher crosslinking degree from the blue light that triggered vinyl group reaction. All four groups of ATES exhibited the mechanical properties comparable to myocardial, breast, muscle, and artery tissues.[89–91] The mechanical properties of bioprinted ATESs could be further altered by tuning hydrogels concentration, functional group modification degree, and crosslinking degree, to make these scaffolds applicable to a broader range of organs and tissues.

Pore size and its distribution within 3D scaffold structures dictate their mass transport properties, which would be essential in determining oxygen and nutrient accessibility of cells within the 3D matrix, as well as the ability of cells to migrate

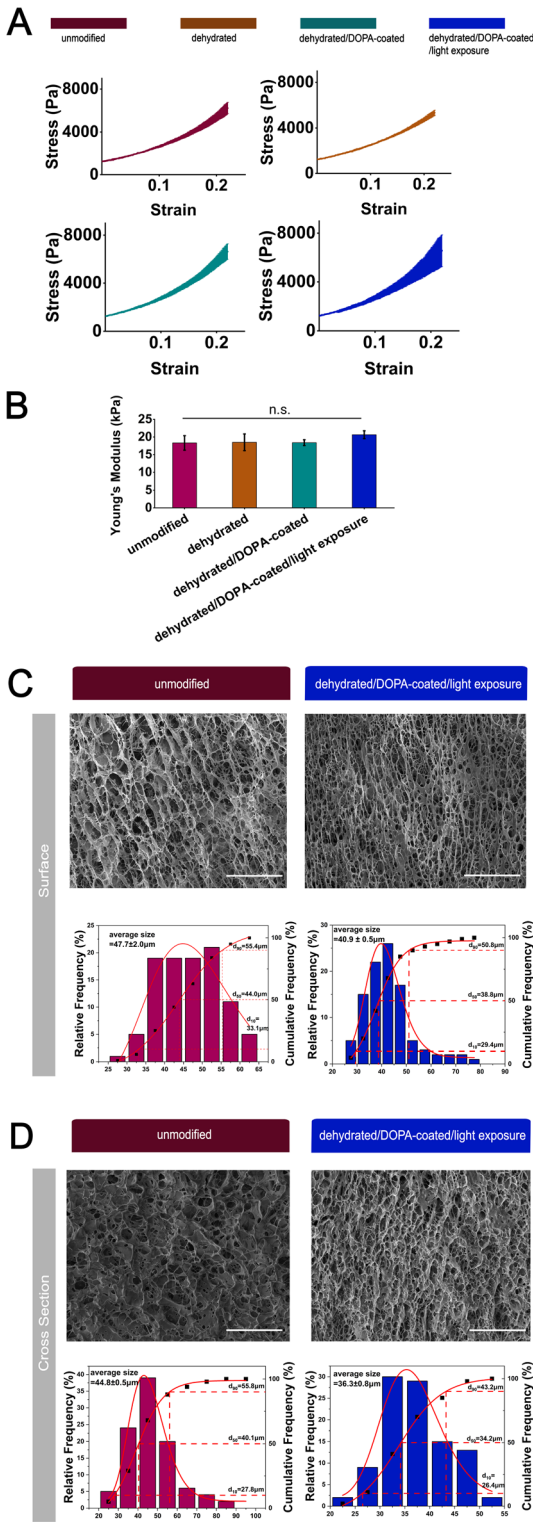

Fig. 4 Mechanical characterization and pore size analysis of 3D bioprinted adhesive tissue engineering scaffolds (ATESs). (A) Strain–stress curves of ATESs obtained from compression test. (B) The Young's modulus for various ATES groups, measured at 9–11% of displacement interval (n = 4). (C) and (D) Scanning electron microscopy (SEM) images and analysis of pore size distribution on the scaffold surface (C) and at the cross-section (D) of constructs. Scale bars represent 100 μm (n = 100).

within the scaffold and remodel/synthesize the ECM.[92–94] These features would, therefore, influence tissue adhesion properties of ATES systems. SEM imaging demonstrated relatively smaller pore sizes on the surface of dehydrated/DOPA-coated/photo-activated scaffolds (an average of 40.9 ± 0.5 μm), in comparison to the unmodified scaffolds (47.7 ± 2.0 μm) (Fig. 4C). The d_{10}, d_{50}, and d_{90} values for the surface pores of the dehydrated/DOPA-coated/photo-activated scaffolds were measured at 29.4 μm, 38.8 μm, and 50.8 μm, respectively, while these values for the unmodified scaffold were 33.1 μm, 44.0 μm, and 55.4 μm, respectively (Fig. 4C). The reduced surface pore diameters in the treated ATES group could possibly be the result of surface dehydration procedure. In addition, the average pore size of the scaffolds' cross-section was measured at 44.8 ± 0.5 μm and 36.3 ± 0.8 μm for the unmodified and modified groups, respectively (Fig. 4D). The cross sectional d_{10}, d_{50}, and d_{90} values were 27.8 μm, 40.1 μm, and 55.8 μm for unmodified group, and 26.4 μm, 34.2 μm, and 43.2 μm, for the modified group, respectively (Fig. 4D). The average pore sizes and their distributions for both scaffold groups were within the acceptable range for TE scaffolds (~5 to hundreds of μm), indicating that the procedures to improve the adhesive properties of bioprinted scaffolds did not compromise their mass transport characteristics.

While obtaining adequate levels of printability, adhesive strength, as well as mechanical and mass transport properties in the developed ATESs is of great importance, the critical requirement for such systems is maintaining proper biocompatibility and bioactivity. The cytotoxicity of the 3D bioprinted ATESs was determined by culturing mouse fibroblasts with the media extracts obtained from various scaffold groups and measuring cell viability using the CCK-8 assay (Fig. 5A). The OD ratios for the unmodified, dehydrated, dehydrated/DOPA-coated, and dehydration/DOPA-coated/photo-activated groups at day 1 were 1.0 ± 0.0, 0.8 ± 0.2, 0.6 ± 0.1, and 1.0 ± 0.3, respectively, and at day 3 were 1.8 ± 0.5, 1.6 ± 0.5, 1.2 ± 0.3, and 1.3 ± 0.3, respectively (Fig. 5B). On day 1, the dehydrated/DOPA-coated/photo-activated ATES group, which had the highest adhesive properties, exhibited an OD ratio approaching 1, indicating negligible cytotoxicity of the extractions obtained from this group. On day 3, the OD ratios of all groups were >1, indicating that the ATES extractions were able to support cell growth for a longer period.

We also seeded the fibroblasts directly onto the surface of various ATES groups and examined cytotoxicity *via* the Live/Dead assay (Fig. 5C). The Live/Dead staining on both days 1 and 3 indicated a substantial high number of live cells (compared with red-stained dead cells), and a significant increase in the number of live cells over the duration of culture (Fig. 5D). These qualitative results confirmed the capacity of bioprinted ATES systems to support cell growth and proliferation. The results from unmodified ATES suggested that the hybrid bioink components yielded minimal cytotoxicity, and results from the dehydrated/DOPA-coated/photo-activated group indicated that the functionalization and modification procedures conducted to enhance adhesive strength,

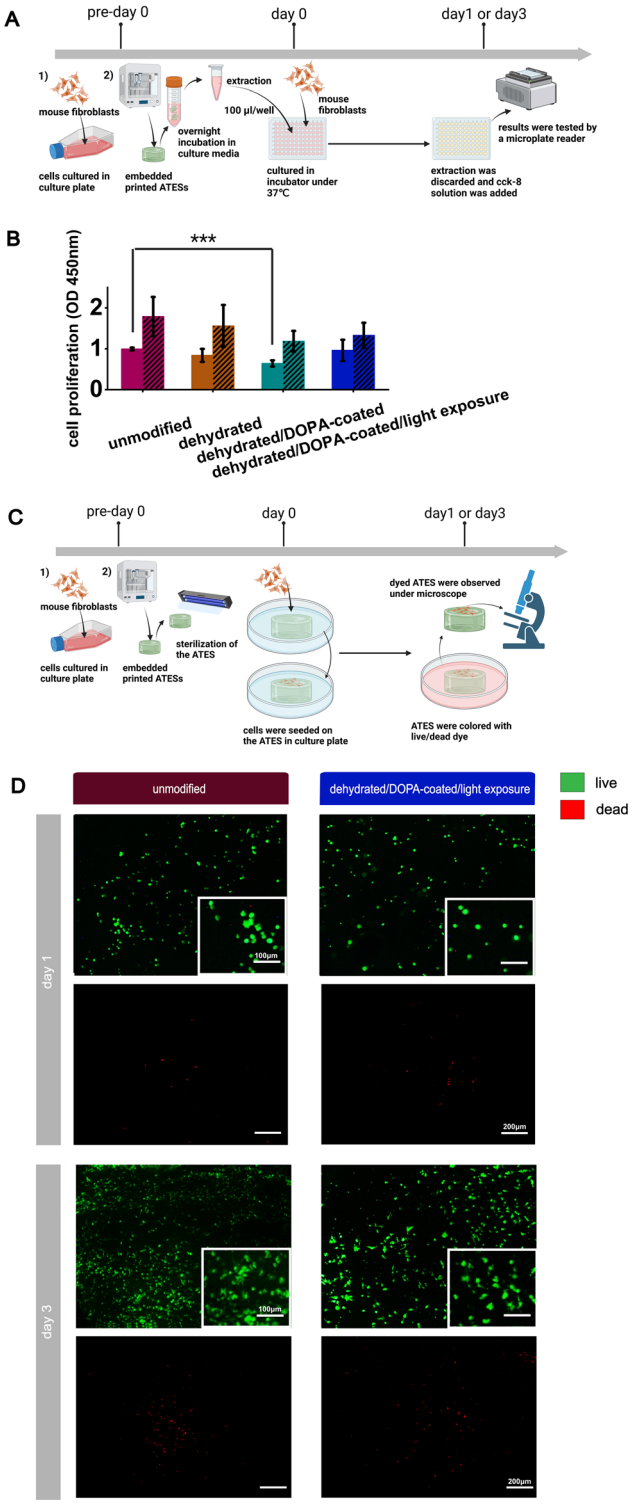

Fig. 5 Biocompatibility analysis of 3D bioprinted adhesive tissue engineered scaffold (ATES) constructs. (A) Schematic illustration of the experimental set-up to assess extraction media toxicity *via* cell counting kit (CCK-8) assay. (B) The optical density (OD) ratio, representing mouse fibroblast viability and proliferation, cultured with the extraction media collected from various groups (n = 4). *p < 0.05, **p < 0.01, and ***p < 0.001. (C) Schematic illustration of the Live/Dead experiment timeline, conducted by direct seeding and culture of mouse fibroblasts onto various ATES constructs. (D) The results of Live/Dead staining of fibroblasts cultured on the surface of bioprinted scaffolds.

caused minimal interference with the bioactivity of these scaffolds.

Following extensive and in-depth *in vitro* characterization of ATES systems, we evaluated the adhesive properties and function of bioprinted scaffolds, as cardiac patch, in a mouse model of MI (Fig. 6). The ATES group treated with dehydration/DOPA-coating/photo-activation was used in the *in vivo* studies, since this group yielded the optimal combination of adhesive properties, as well as other physiomechanical and biological features. The characterization of adhesive properties of ATES *in vivo*, on the surface of heart tissue, was challenging due to several factors. First, body fluids and blood covered the surface of the heart, and it was difficult to thoroughly remove these fluids prior to ATES application. The wet surface could affect the adhesion processes as the water molecules establish a barrier between the functional groups on the surface of ATES and the myocardial tissue, inhibiting the effective engraftment.[95] In addition, due to the heart beating, dynamic forces

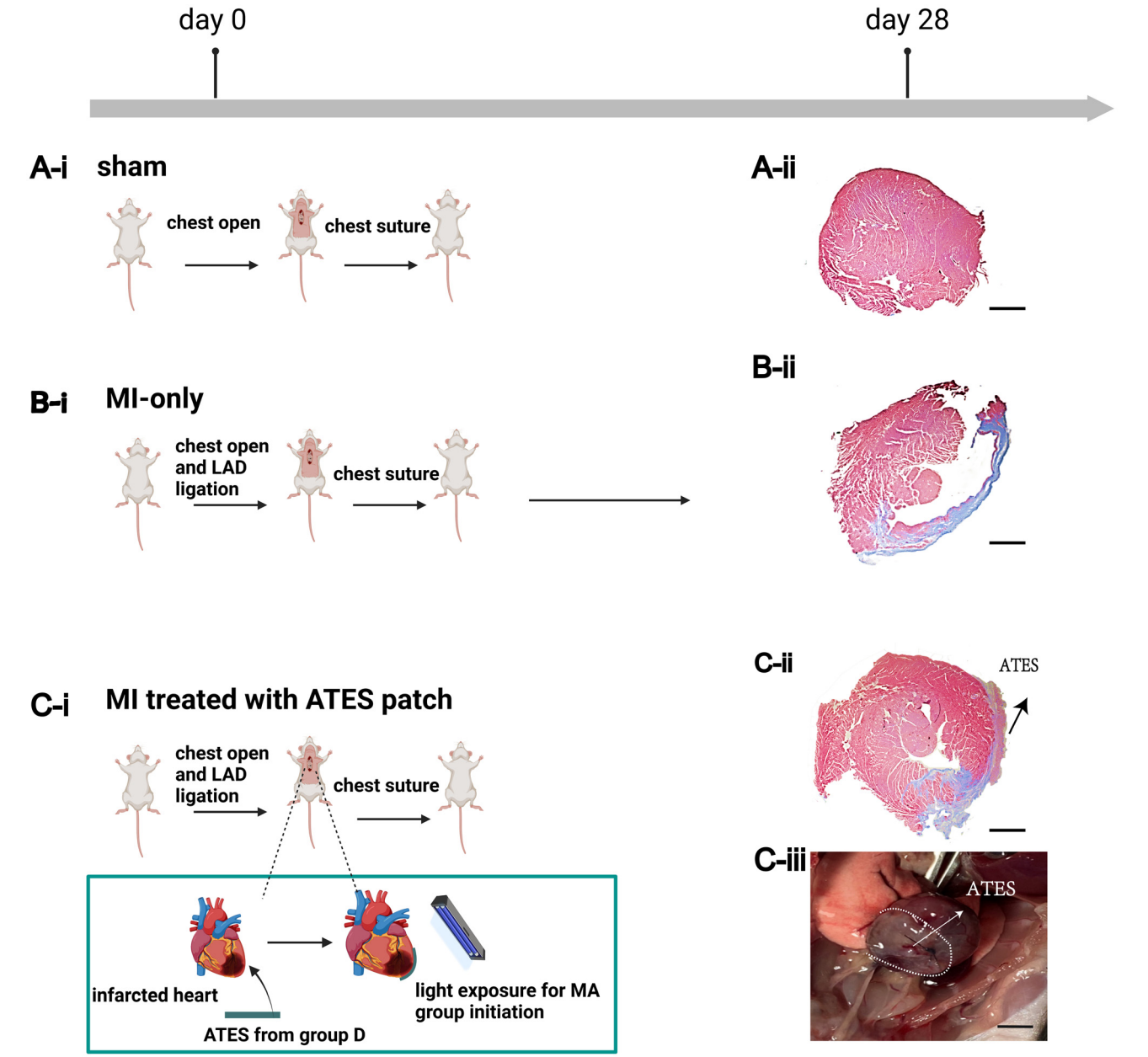

Fig. 6 Evaluation of the *in vivo* function of adhesive tissue engineering scaffolds (ATESs) in a mouse model of myocardial infarction (MI). (A) The experimental procedure (A-i) and the Masson's trichrome staining image (A-ii) of the sham animals (control, no MI and no patch). (B) The experimental procedure (B-i) and the Masson's trichrome staining image (B-ii) of the MI-only animals (no patch). (C) The experimental procedure (C-i), the Masson's trichrome staining image (C-ii), and the photo of treated heart (C-iii) of the MI mice, treated with the bioprinted ATES patches. Histological examination of all groups was conducted at the end of 4-week study. Scale bars represent 1 mm.

would be exerted to the scaffold, which could affect its bonding to the heart. Further, the formation of damaged myocardium (MI) causes an inflamed environment. Free radicals, oxidative stress, and pH fluctuations might influence the cohesive strength, degradation rate, swelling behavior, and adhesive properties of the ATESs, particularly in the long term.[96] For instance, under low pH environment, amines on the tissue surface would be inhibited by amine protonation, hence impeding the interactions between the amine groups and functional groups of ATES, which may, in turn, diminish the adhesive strength.[96]

Grafted ATES remained fully adhered to the heart tissue after four weeks (typical duration of cardia patch studies in small animal models), suggesting adequate adhesive strengths of the patch for *in vivo* applications (Fig. 6C-ii and iii, indicated by the arrow). Masson's trichrome staining of heart sections at the end of 4-week study also demonstrated the noticeable effect of ATES patch in reducing the fibrosis, in comparison to the control group without patch (Fig. 6B). This highlighted the potential impact of ATES, by providing mechanical support, of diminishing the adverse cardiac remodeling post MI. Future research could be conducted to investigate the role of ATESs in the treatment of myocardial infarction and other illnesses. In this work, the *in vivo* adhesion property of the ATESs under harsh conditions, such as under dynamic stresses, inflamed environment,[97–99] and moist milieu, was the primary interest.

Tissue engineering scaffolds (TESs) had been used as functional platform for cell growth and tissue regeneration.[100] Recent years, adhesive TESs (ATESs)[101–103] were proposed as a new generation of strategy for tissue engineering to avoid secondary damage of suturing[104] and toxicity or side effects of traditional bio-glue.[18,105] In our recently published review,[106] ATESs applied to various tissues and organs were discussed in details. However, those ATESs were generally formed from *in situ* solidified pre-gel solutions casted or injected to the recipient tissue,[103] which lack the probability of being tailored into desired geometry and structure. We recently reported the first generation of internal and external shape designable ATESs fabricated by both air printing and FRESH printing (embedded printing) technology.[107] The adhesion strength of ATESs from the embedded printing method was not high enough to be applied *in vivo* for clinical application. And while the adhesion property of ATESs from the air printing method was much higher, the method requires sophisticated equipment and operation when being used for clinical application. It is essential to investigate a method to develop 3D printed ATESs with both high adhesion property to have *in vivo* application potential, as well as accessible and easy fabrication process for clinical application.

In this study, a brand new method to develop 3D printed ATESs through FRESH printing method was proposed. The protocol allows easy fabrication and application process for the ATESs, which could be stored as an off-the-shelf product to be used in surgery. The *in vitro* adhesion strength was tested and the results suggested that after post-printing modifications, the adhesion property of ATESs improved. *In vivo* adhesion property was studied in a mouse model of myocardial infarction. The results suggested that the ATESs developed in this study had both *in vivo* application potential, as well as accessible and easy fabrication process. Properties such as mechanical property, swelling behavior, pore sizes and its distribution, and cytotoxicity were examined and the studies suggested that strategies to improve the adhesion property of ATESs would not affect the cell supporting function. Printing fidelity under micro and bulk scale were examined and the results demonstrated relatively high printing accuracy. The design and protocol that was proposed in the study provided a method to fabricate shape designable ATESs with *in vivo* application potential, convenient fabrication and application process, cell support function, as well as relatively high printing accuracy.

In this study, we overcame the difficulty of improving the adhesion property of ATESs after 3D printing and solidification, and provided, for the first time, 3D printed shape designable functional ATESs with convenient *in vivo* application potential. In future studies, complex internal and external design, including vessel system,[108,109] personalized structures[110,111] and tissue imitations,[112,113] were to be printed. Also, comprehensive studies to investigate the ATESs system for tissue regeneration application, such as myocardial infarction, were to be conducted in order for future clinical translation.

Conclusions

This study introduced a new generation of 3D bioprinted ATES systems with adequate adhesive properties, together with optimal biofabrication workflow, physiomechanical, and biological function both *in vitro* and *in vivo*. The HAMA-tyr, GelMA, and gelatin components were used to form a hybrid bioink formulation. An optimized embedded 3D bioprinting technique was used to fabricate the ATES systems at adequate micro- and macro-scale fidelity levels, while maintaining the targeted adhesive properties. Post-printing modifications such as dopamine coating, surface dehydration and light exposure significantly improved the adhesive strength of the scaffold both *in vitro* (in the dry and wet states) and *in vivo*, in the mouse model of MI.

Future studies could further investigate the quantitative impact of ATES as cardiac patch in restoring the cardiac structure and function post MI, using echocardiography, cardiac MRI, and in-depth immunohistochemical assays. Further, comparing conventional patch grafting techniques, such as suturing, with the self-adhesion of ATESs would shed light into potential advantages of the latter technique, by minimizing excessive damage to the heart and enhancing engraftment/integration of the patch with the host tissue. Considering the advanced bioprinting method used to create these patch constructs, future works could focus on tailoring the ATES geometry to create patient and damage specific cardiac patch

devices.[114,115] Also, complex vascular networks could be printed within the patch to further enhance the blood perfusion and, hence, the regenerative function of ATES systems.[70,116,117]

Ethical statement

All animal procedures were performed in accordance with the Guidelines for Care and Use of Laboratory Animals of Peking University and approved by the Animal Ethics Committee of Institutional Animal Care and Use Committee (IACUC) of Peking University.

Data availability

This is to confirm that the data presented in this manuscript have been already included in the main file of the manuscript.

Conflicts of interest

There are no conflicts of interest to declare.

Acknowledgements

The work was supported by the National Natural Science Foundation of China (No. 82070286) and the National Key Research and Development Program of China (Project No. 2016YFC1101301).

References

1 B. P. Chan and K. W. Leong, Scaffolding in tissue engineering: general approaches and tissue-specific considerations, *Eur. Spine J.*, 2008, **17**(Suppl. 4), 467–479.
2 A. A. M. Shimojo, *et al.*, *Scaffolds for Tissue Engineering: A State-of-the-Art Review Concerning Types, Properties, Materials, Processing, and Characterization*, 2020.
3 A. S. Theus, *et al.*, Biomaterial approaches for cardiovascular tissue engineering, *Emergent Mater.*, 2019, **2**(2), 193–207.
4 M. Hosseinkhani, *et al.*, Tissue engineered scaffolds in regenerative medicine, *World J. Plast. Surg.*, 2014, **3**(1), 3–7.
5 S. M. Wu and V. Serpooshan, Cardiovascular Regenerative Medicine: Challenges, Perspectives, and Future Directions, in *Cardiovascular Regenerative Medicine: Tissue Engineering and Clinical Applications*, ed. V. Serpooshan and S. M. Wu, Springer International Publishing, Cham; 2019, pp. 223–225.
6 M. L. Tomov, *et al.*, Engineering Functional Cardiac Tissues for Regenerative Medicine Applications, *Curr. Cardiol. Rep.*, 2019, **21**(9), 105.
7 L. Suamte, *et al.*, Various manufacturing methods and ideal properties of scaffolds for tissue engineering applications, *Smart Mater. Manuf.*, 2023, **1**, 100011.
8 S. J. Hollister, R. D. Maddox and J. M. Taboas, Optimal design and fabrication of scaffolds to mimic tissue properties and satisfy biological constraints, *Biomaterials*, 2002, **23**(20), 4095–4103.
9 M. J. Hill, M. Mahmoudi and P. P. S. S. Abadi, Nanobiomaterial Advances in Cardiovascular Tissue Engineering, in *Cardiovascular Regenerative Medicine: Tissue Engineering and Clinical Applications*, ed. V. Serpooshan and S. M. Wu, Springer International Publishing, Cham, 2019, pp. 79–106.
10 E. B. Hunziker and A. Stahli, Surgical suturing of articular cartilage induces osteoarthritis-like changes, *Osteoarthritis Cartilage*, 2008, **16**(9), 1067–1073.
11 V. Serpooshan, *et al.*, The effect of bioengineered acellular collagen patch on cardiac remodeling and ventricular function post myocardial infarction, *Biomaterials*, 2013, **34**(36), 9048–9055.
12 V. Serpooshan and P. Ruiz-Lozano, Ultra-rapid manufacturing of engineered epicardial substitute to regenerate cardiac tissue following acute ischemic injury, *Methods Mol. Biol.*, 2014, **1210**, 239–248.
13 K. Wei, *et al.*, Epicardial FSTL1 reconstitution regenerates the adult mammalian heart, *Nature*, 2015, **525**(7570), 479–485.
14 K. Zheng, *et al.*, Recent progress in surgical adhesives for biomedical applications, *Smart Mater. Med.*, 2022, **3**, 41–65.
15 S. Chen, *et al.*, Adhesive Tissue Engineered Scaffolds: Mechanisms and Applications, *Front. Bioeng. Biotechnol.*, 2021, **9**, 683079.
16 S. Tarafder, *et al.*, Bioadhesives for musculoskeletal tissue regeneration, *Acta Biomater.*, 2020, **117**, 77–92.
17 Z. Ma, G. Bao and J. Li, Multifaceted Design and Emerging Applications of Tissue Adhesives, *Adv. Mater.*, 2021, e2007663.
18 G. Pascual, *et al.*, Cytotoxicity of Cyanoacrylate-Based Tissue Adhesives and Short-Term Preclinical In Vivo Biocompatibility in Abdominal Hernia Repair, *PLoS One*, 2016, **11**(6), e0157920.
19 W. D. Spotnitz, Fibrin Sealant: The Only Approved Hemostat, Sealant, and Adhesive-a Laboratory and Clinical Perspective, *ISRN Surg.*, 2014, **2014**, 203943.
20 C. S. Russell, *et al.*, In Situ Printing of Adhesive Hydrogel Scaffolds for the Treatment of Skeletal Muscle Injuries, *ACS Appl. Bio Mater.*, 2020, **3**(3), 1568–1579.
21 M. Ark, *et al.*, Characterisation of a novel light activated adhesive scaffold: Potential for device attachment, *J. Mech. Behav. Biomed. Mater.*, 2016, **62**, 433–445.
22 D. Wu, *et al.*, Highly Adhesive Amyloid-Polyphenol Hydrogels for Cell Scaffolding, *Biomacromolecules*, 2023, **24**(1), 471–480.
23 Y. He, *et al.*, A smart adhesive Janus hydrogel for non-invasive cardiac repair and tissue adhesion prevention, *Nat. Commun.*, 2022, **13**(1), 7666.

24 C. Salzlechner, *et al.*, Adhesive Hydrogels for Maxillofacial Tissue Regeneration Using Minimally Invasive Procedures, *Adv. Healthcare Mater.*, 2020, **9**(4), e1901134.
25 Y. Hou, *et al.*, A fast UV-curable PU-PAAm hydrogel with mechanical flexibility and self-adhesion for wound healing, *RSC Adv.*, 2020, **10**(9), 4907–4915.
26 B. Saleh, *et al.*, Local Immunomodulation Using an Adhesive Hydrogel Loaded with miRNA-Laden Nanoparticles Promotes Wound Healing, *Small*, 2019, **15**(36), e1902232.
27 S. H. Kim, *et al.*, Enzyme-mediated tissue adhesive hydrogels for meniscus repair, *Int. J. Biol. Macromol.*, 2018, **110**, 479–487.
28 I. Strehin, *et al.*, A versatile pH sensitive chondroitin sulfate-PEG tissue adhesive and hydrogel, *Biomaterials*, 2010, **31**(10), 2788–2797.
29 A. E. Jakus, A. L. Rutz and R. N. Shah, Advancing the field of 3D biomaterial printing, *Biomed. Mater.*, 2016, **11**(1), 014102.
30 S. V. Murphy and A. Atala, 3D bioprinting of tissues and organs, *Nat. Biotechnol.*, 2014, **32**(8), 773–785.
31 Y. S. Zhang, *et al.*, 3D Bioprinting for Tissue and Organ Fabrication, *Ann. Biomed. Eng.*, 2017, **45**(1), 148–163.
32 A. Cetnar, *et al.*, *3D Bioprinting in Clinical Cardiovascular Medicine*, in *3D Bioprinting in Medicine: Technologies, Bioinks, and Applications*, ed. M. Guvendiren, Springer International Publishing, Cham, 2019, p. 149–162.
33 V. Serpooshan and M. Guvendiren, Editorial for the Special Issue on 3D Printing for Tissue Engineering and Regenerative Medicine, *Micromachines*, 2020, **11**(4), 366.
34 S. J. Wu, *et al.*, A 3D printable tissue adhesive, *Nat. Commun.*, 2024, **15**(1), 1215.
35 P. Wei, *et al.*, A 3D printed biomimetic scaffold for cartilage regeneration with lubrication, load-bearing, and adhesive fixation properties, *Tribol. Int.*, 2024, **192**, 109328.
36 H. Cui, *et al.*, 3D Bioprinting for Organ Regeneration, *Adv. Healthcare Mater.*, 2017, **6**(1), 1601118.
37 C. J. Gil, *et al.*, Leveraging 3d Bioprinting And Photon-Counting Computed Tomography to Enable Noninvasive Quantitative Tracking of Multifunctional Tissue Engineered Constructs, *Adv. Healthcare Mater.*, 2023, e2302271.
38 L. Li, *et al.*, Methacrylate-Modified Gold Nanoparticles Enable Non-Invasive Monitoring of Photocrosslinked Hydrogel Scaffolds, *Adv. NanoBiomed Res.*, 2022, **2**(7), 2200022.
39 C. Gil, *et al.*, Abstract MP207: A Precision Medicine Approach For Non-invasive, Longitudinal, And Quantitative Monitoring Of Cardiac Tissue-engineered Scaffolds, *Circ. Res.*, 2021, **129**(Suppl_1), AMP207.
40 A. A. de la Lastra, *et al.*, Tissue Engineering Scaffolds Fabricated in Dissolvable 3D-Printed Molds for Patient-Specific Craniofacial Bone Regeneration, *J. Funct. Biomater.*, 2018, **9**(3), 46.
41 D. J. Shiwarski, *et al.*, Emergence of FRESH 3D printing as a platform for advanced tissue biofabrication, *APL Bioeng.*, 2021, **5**(1), 010904.
42 T. Bhattacharjee, *et al.*, Writing in the granular gel medium, *Sci. Adv.*, 2015, **1**(8), e1500655.
43 T. J. Hinton, *et al.*, Three-dimensional printing of complex biological structures by freeform reversible embedding of suspended hydrogels, *Sci. Adv.*, 2015, **1**(9), e1500758.
44 L. Ning and X. Chen, A brief review of extrusion-based tissue scaffold bio-printing, *Biotechnol. J.*, 2017, **12**(8), 1600671.
45 L. Ning, *et al.*, Embedded 3D Bioprinting of Gelatin Methacryloyl-Based Constructs with Highly Tunable Structural Fidelity, *ACS Appl. Mater. Interfaces*, 2020, **12**(40), 44563–44577.
46 L. Ning, *et al.*, Biomechanical factors in three-dimensional tissue bioprinting, *Appl. Phys. Rev.*, 2020, **7**(4), 041319.
47 A. S. Theus, *et al.*, Bioprintability: Physiomechanical and Biological Requirements of Materials for 3D Bioprinting Processes, *Polymers*, 2020, **12**(10), 2262.
48 N. Rajabi, *et al.*, Recent Advances on Bioprinted Gelatin Methacrylate-Based Hydrogels for Tissue Repair, *Tissue Eng., Part A*, 2021, **27**(11–12), 679–702.
49 R. Alexa, *et al.*, 3D-Printed Gelatin Methacryloyl-Based Scaffolds with Potential Application in Tissue Engineering, *Polymers*, 2021, **13**(5), 727.
50 M. T. Poldervaart, *et al.*, 3D bioprinting of methacrylated hyaluronic acid (MeHA) hydrogel with intrinsic osteogenicity, *PLoS One*, 2017, **12**(6), e0177628.
51 S. Chen, *et al.*, Abstract P403: Three-dimensional Bioprinting Of Adhesive Cardiac Patch Systems, *Circ. Res.*, 2021, **129**(Suppl_1), AP403.
52 S. Chen, *et al.*, Extrusion-Based 3D Bioprinting of Adhesive Tissue Engineering Scaffolds Using Hybrid Functionalized Hydrogel Bioinks, *Adv. Biol.*, 2023, **7**(7), e2300124.
53 J. Cui, *et al.*, Morphine protects against intracellular amyloid toxicity by inducing estradiol release and upregulation of Hsp70, *J. Neurosci.*, 2011, **31**(45), 16227–16240.
54 S. K. Seidlits, *et al.*, The effects of hyaluronic acid hydrogels with tunable mechanical properties on neural progenitor cell differentiation, *Biomaterials*, 2010, **31**(14), 3930–3940.
55 B. M. Hong, S. A. Park and W. H. Park, Effect of photoinitiator on chain degradation of hyaluronic acid, *Biomater. Res.*, 2019, **23**, 21.
56 E. Sani, *et al.*, Sutureless repair of corneal injuries using naturally derived bioadhesive hydrogels, *Sci. Adv.*, 2019, **5**(3), eaav1281.
57 L. Ning, *et al.*, A 3D Bioprinted in vitro Model of Neuroblastoma Recapitulates Dynamic Tumor-Endothelial Cell Interactions Contributing to Solid Tumor Aggressive Behavior, *Adv. Sci.*, 2022, **9**(23), e2200244.
58 A. S. Theus, *et al.*, 3D bioprinting of nanoparticle-laden hydrogel scaffolds with enhanced antibacterial and imaging properties, *iScience*, 2022, **25**(9), 104947.

59 J. Zhang, *et al.*, Synthesis and characterization of hyaluronic acid/human-like collagen hydrogels, *Mater. Sci. Eng., C*, 2014, **43**, 547–554.
60 X. Zhang, *et al.*, Mussel-inspired antibacterial polydopamine/chitosan/temperature-responsive hydrogels for rapid hemostasis, *Int. J. Biol. Macromol.*, 2019, **138**, 321–333.
61 W. Gao, *et al.*, Ionic Carbazole-Based Water-Soluble Two-Photon Photoinitiator and the Fabrication of Biocompatible 3D Hydrogel Scaffold, *ACS Appl. Mater. Interfaces*, 2021, **13**(24), 27796–27805.
62 T.-D. Zhang, *et al.*, Layer-by-layer coating of polyvinylamine and dopamine-modified hyaluronic acid inhibits the growth of bacteria and tumor cell lines on the surface of materials, *Appl. Surf. Sci.*, 2020, **530**, 147197.
63 Y. Hao, *et al.*, Biological Cardiac Patch Based on Extracellular Vesicles and Extracellular Matrix for Regulating Injury-Related Microenvironment and Promoting Cardiac Tissue Recovery, *ACS Appl. Bio Mater.*, 2022, **5**(11), 5218–5230.
64 V. Bhagat and M. L. Becker, Degradable Adhesives for Surgery and Tissue Engineering, *Biomacromolecules*, 2017, **18**(10), 3009–3039.
65 W. Furst and A. Banerjee, Release of glutaraldehyde from an albumin-glutaraldehyde tissue adhesive causes significant in vitro and in vivo toxicity, *Ann. Thorac. Surg.*, 2005, **79**(5), 1522–1528, discussion 1529.
66 Y. Zhou, *et al.*, Rapid Gelling Chitosan/Polylysine Hydrogel with Enhanced Bulk Cohesive and Interfacial Adhesive Force: Mimicking Features of Epineurial Matrix for Peripheral Nerve Anastomosis, *Biomacromolecules*, 2016, **17**(2), 622–630.
67 L. Koivusalo, *et al.*, Tissue adhesive hyaluronic acid hydrogels for sutureless stem cell delivery and regeneration of corneal epithelium and stroma, *Biomaterials*, 2019, **225**, 119516.
68 B. W. Walker, *et al.*, Engineering a naturally-derived adhesive and conductive cardiopatch, *Biomaterials*, 2019, **207**, 89–101.
69 K. Lei, *et al.*, In Vitro and in Vivo Characterization of a Foam-Like Polyurethane Bone Adhesive for Promoting Bone Tissue Growth, *ACS Biomater. Sci. Eng.*, 2019, **5**(10), 5489–5497.
70 P. Datta, B. Ayan and I. T. Ozbolat, Bioprinting for vascular and vascularized tissue biofabrication, *Acta Biomater.*, 2017, **51**, 1–20.
71 B. Byambaa, *et al.*, Bioprinted Osteogenic and Vasculogenic Patterns for Engineering 3D Bone Tissue, *Adv. Healthcare Mater.*, 2017, **6**(16), 1700015.
72 J. B. Robbins, *et al.*, A novel in vitro three-dimensional bioprinted liver tissue system for drug development, *FASEB J.*, 2013, **27**(S1), 872.12–872.12.
73 Y. Huang, *et al.*, Molecular aspects of muco- and bioadhesion:: Tethered structures and site-specific surfaces, *J. Controlled Release*, 2000, **65**(1), 63–71.
74 L. Han, *et al.*, Mussel-Inspired Tissue-Adhesive Hydrogel Based on the Polydopamine-Chondroitin Sulfate Complex for Growth-Factor-Free Cartilage Regeneration, *ACS Appl. Mater. Interfaces*, 2018, **10**(33), 28015–28026.
75 Y. Hou, X. Deng and C. Xie, Biomaterial surface modification for underwater adhesion, *Smart Mater. Med.*, 2020, **1**, 77–91.
76 D. X. Oh, *et al.*, Surface forces apparatus and its applications for nanomechanics of underwater adhesives, *Korean J. Chem. Eng.*, 2014, **31**(8), 1306–1315.
77 Y.-W. Ding, *et al.*, Recent advances in hyaluronic acid-based hydrogels for 3D bioprinting in tissue engineering applications, *Smart Mater. Med.*, 2023, **4**, 59–68.
78 P. Song, *et al.*, DLP fabricating of precision GelMA/HAp porous composite scaffold for bone tissue engineering application, *Composites, Part B*, 2022, **244**, 110163.
79 H. Shirahama, *et al.*, Precise Tuning of Facile One-Pot Gelatin Methacryloyl (GelMA) Synthesis, *Sci. Rep.*, 2016, **6**, 31036.
80 Y.-Z. Yu, *et al.*, Fabrication of hierarchical polycaprolactone/gel scaffolds via combined 3D bioprinting and electrospinning for tissue engineering, *Adv. Manuf.*, 2014, **2**(3), 231–238.
81 M. A. Cadena, *et al.*, A 3D Bioprinted Cortical Organoid Platform for Modeling Human Brain Development, *Adv. Healthcare Mater.*, 2024, 2401603.
82 A. Schwab, *et al.*, Printability and Shape Fidelity of Bioinks in 3D Bioprinting, *Chem. Rev.*, 2020, **120**(19), 11028–11055.
83 L. Han, *et al.*, Mussel-Inspired Tissue-Adhesive Hydrogel Based on the Polydopamine–Chondroitin Sulfate Complex for Growth-Factor-Free Cartilage Regeneration, *ACS Appl. Mater. Interfaces*, 2018, **10**(33), 28015–28026.
84 S. M. Bittner, *et al.*, Swelling Behaviors of 3D Printed Hydrogel and Hydrogel-Microcarrier Composite Scaffolds, *Tissue Eng., Part A*, 2021, **27**(11–12), 665–678.
85 K. Nakamae, T. Miyata and A. S. Hoffman, Swelling behavior of hydrogels containing phosphate groups, *Makromol. Chem.*, 1992, **193**(4), 983–990.
86 M. L. Vueba, *et al.*, Influence of cellulose ether polymers on ketoprofen release from hydrophilic matrix tablets, *Eur. J. Pharm. Biopharm.*, 2004, **58**(1), 51–59.
87 V. S. Praptowidodo, Influence of swelling on water transport through PVA-based membrane, *J. Mol. Struct.*, 2005, **739**(1), 207–212.
88 C. M. Murphy, *et al.*, Mesenchymal stem cell fate is regulated by the composition and mechanical properties of collagen-glycosaminoglycan scaffolds, *J. Mech. Behav. Biomed. Mater.*, 2012, **11**, 53–62.
89 S. Budday, *et al.*, Fifty Shades of Brain: A Review on the Mechanical Testing and Modeling of Brain Tissue, *Arch. Comput. Methods Eng.*, 2020, **27**(4), 1187–1230.
90 J. Munch and S. Abdelilah-Seyfried, Sensing and Responding of Cardiomyocytes to Changes of Tissue Stiffness in the Diseased Heart, *Front. Cell Dev. Biol.*, 2021, **9**, 642840.
91 R. Schleip, *et al.*, Passive muscle stiffness may be influenced by active contractility of intramuscular connective tissue, *Med. Hypotheses*, 2006, **66**(1), 66–71.

92 G. Lutzweiler, The Overview of Porous, Bioactive Scaffolds as Instructive Biomaterials for Tissue Regeneration and Their Clinical Translation, *Pharmaceutics*, 2020, **12**(7), 602.
93 V. Serpooshan, *et al.*, Fibroblast contractility and growth in plastic compressed collagen gel scaffolds with microstructures correlated with hydraulic permeability, *J. Biomed. Mater. Res., Part A*, 2011, **96**(4), 609–620.
94 V. Serpooshan, *et al.*, Reduced hydraulic permeability of three-dimensional collagen scaffolds attenuates gel contraction and promotes the growth and differentiation of mesenchymal stem cells, *Acta Biomater.*, 2010, **6**(10), 3978–3987.
95 H. Y. Yuen, H. P. Bei and X. Zhao, Underwater and wet adhesion strategies for hydrogels in biomedical applications, *Chem. Eng. J.*, 2022, **431**, 133372.
96 G. M. Taboada, *et al.*, Overcoming the translational barriers of tissue adhesives, *Nat. Rev. Mater.*, 2020, **5**(4), 310–329.
97 N. G. Frangogiannis, C. W. Smith and M. L. Entman, The inflammatory response in myocardial infarction, *Cardiovasc. Res.*, 2002, **53**(1), 31–47.
98 N. G. Frangogiannis, Regulation of the inflammatory response in cardiac repair, *Circ. Res.*, 2012, **110**(1), 159–173.
99 I. Kologrivova, *et al.*, Cells of the immune system in cardiac remodeling: main players in resolution of inflammation and repair after myocardial infarction, *Front. Immunol.*, 2021, **12**, 664457.
100 A. A. M. Shimojo, *et al.*, Scaffolds for tissue engineering: A state-of-the-art review concerning types, properties, materials, processing, and characterization, *Racing for the surface: Antimicrobial and Interface tissue engineering*, 2020, pp. 647–676.
101 C. S. Russell, *et al.*, In situ printing of adhesive hydrogel scaffolds for the treatment of skeletal muscle injuries, *ACS Appl. Bio Mater.*, 2020, **3**(3), 1568–1579.
102 M. Ark, *et al.*, Characterisation of a novel light activated adhesive scaffold: potential for device attachment, *J. Mech. Behav. Biomed. Mater.*, 2016, **62**, 433–445.
103 D. Wu, *et al.*, Highly adhesive amyloid–polyphenol hydrogels for cell scaffolding, *Biomacromolecules*, 2022, **24**(1), 471–480.
104 E. B. Hunziker and A. Stähli, Surgical suturing of articular cartilage induces osteoarthritis-like changes, *Osteoarthritis Cartilage*, 2008, **16**(9), 1067–1073.
105 W. D. Spotnitz, Fibrin sealant: the only approved hemostat, sealant, and adhesive—a laboratory and clinical perspective, *Int. Sch. Res. Notices.*, 2014, (1), 203943.
106 S. Chen, *et al.*, Adhesive tissue engineered scaffolds: mechanisms and applications, *Front. Bioeng. Biotechnol.*, 2021, **9**, 683079.
107 S. Chen, *et al.*, Extrusion–based 3D bioprinting of adhesive tissue engineering scaffolds using hybrid functionalized hydrogel bioinks, *Adv. Biol.*, 2023, **7**(7), 2300124.
108 M. L. Tomov, *et al.*, *3D bioprinting of cardiovascular tissue constructs: cardiac bioinks*, *Cardiovascular Regenerative Medicine: Tissue Engineering and Clinical Applications*, 2019, pp. 63–77.
109 P. Datta, B. Ayan and I. T. Ozbolat, Bioprinting for vascular and vascularized tissue biofabrication, *Acta Biomater.*, 2017, **51**, 1–20.
110 N. Matthews, *et al.*, Taking it personally: 3D bioprinting a patient-specific cardiac patch for the treatment of heart failure, *Bioengineering*, 2022, **9**(3), 93.
111 A. A. De la Lastra, *et al.*, Tissue engineering scaffolds fabricated in dissolvable 3D-printed molds for patient-specific craniofacial bone regeneration, *J. Funct. Biomater.*, 2018, **9**(3), 46.
112 B. Byambaa, *et al.*, Bioprinted osteogenic and vasculogenic patterns for engineering 3D bone tissue, *Adv. Healthcare Mater.*, 2017, **6**(16), 1700015.
113 J. B. Robbins, *et al.*, A novel in vitro three-dimensional bioprinted liver tissue system for drug development, *FASEB J.*, 2013, **27**(872), 812.
114 N. Matthews, *et al.*, Taking It Personally: 3D Bioprinting a Patient-Specific Cardiac Patch for the Treatment of Heart Failure, *Bioengineering*, 2022, **9**(3), 93.
115 C. Gardin, *et al.*, Recent Applications of Three Dimensional Printing in Cardiovascular Medicine, *Cells*, 2020, **9**(3), 742.
116 V. Serpooshan and J. Zhang, in *Advanced Technologies in Cardiovascular Bioengineering*, Springer, Cham., Switzerland, 1st edn, 2022, pp. 407.
117 M. L. Tomov, *et al.*, *3D Bioprinting of Cardiovascular Tissue Constructs: Cardiac Bioinks*, in *Cardiovascular Regenerative Medicine: Tissue Engineering and Clinical Applications*, ed. V. Serpooshan and S. M. Wu, Springer International Publishing, Cham, 2019, pp. 63–77.

